New Upper Limit on the Axion-Photon Coupling with an Extended CAST Run with a Xe-Based Micromegas Detector

K. Altenmüller,[1] V. Anastassopoulos,[2] S. Arguedas-Cuendis,[3] S. Aune,[4] J. Baier,[5] K. Barth,[3] H. Bräuninger,[6,‡] G. Cantatore,[7] F. Caspers,[3,8] J. F. Castel,[1] S. A. Çetin,[9] F. Christensen,[10] C. Cogollos,[11,1] T. Dafni,[1] M. Davenport,[3] T. A. Decker,[12] K. Desch,[13] D. Díez-Ibáñez,[1] B. Döbrich,[3] E. Ferrer-Ribas,[4] H. Fischer,[5] W. Funk,[3] J. Galán,[1] J. A. García,[1] A. Gardikiotis,[14] I. Giomataris,[4] J. Golm,[3,15] C. H. Hailey,[16] M. D. Hasinoff,[17] D. H. H. Hoffmann,[18] I. G. Irastorza,[1] J. Jacoby,[5] A. C. Jakobsen,[10] K. Jakovčić,[19] J. Kaminski,[13] M. Karuza,[20,21] S. Kostoglou,[3] C. Krieger,[22] B. Lakić,[19,‡] J. M. Laurent,[3] G. Luzón,[1] C. Malbrunot,[3] C. Margalejo[1,*] M. Maroudas,[23] L. Miceli,[24] H. Mirallas,[1] P. Navarro,[25] L. Obis,[1] A. Özbey,[9,26] K. Özbozduman,[9,27] T. Papaevangelou,[4] O. Pérez,[1] M. J. Pivovaroff,[12] M. Rosu,[28] E. Ruiz-Chóliz,[1] J. Ruz,[12,1,†] S. Schmidt,[13] M. Schumann,[5] Y. K. Semertzidis,[24,29] S. K. Solanki,[30] L. Stewart,[3] T. Vafeiadis,[3] J. K. Vogel,[12,1] and K. Zioutas[3,2]

(CAST Collaboration)

[1]*Centro de Astropartículas y Física de Altas Energías (CAPA) and Departamento de Física Teórica, University de Zaragoza, 50009—Zaragoza, Spain*
[2]*Physics Department, University of Patras, Patras, Greece*
[3]*European Organization for Nuclear Research (CERN), 1211 Geneva 23, Switzerland*
[4]*IRFU, CEA, Université Paris-Saclay, 91191 Gif-sur-Yvette, France*
[5]*Physikalisches Institut, Albert-Ludwigs-Universität Freiburg, 79104 Freiburg, Germany*
[6]*Max-Planck-Institut für Extraterrestrische Physik, Garching, Germany*
[7]*University of Trieste and Instituto Nazionale di Fisica Nucleare (INFN), Sezione di Trieste, Trieste, Italy*
[8]*European Scientific Institute, Archamps, France*
[9]*Istinye University, Institute of Sciences, 34396, Sariyer, Istanbul, Turkey*
[10]*DTU Space, National Space Institute, Technical University of Denmark, 2800 Lyngby, Denmark*
[11]*Institut de Ciències del Cosmos, Universitat de Barcelona (UB-IEEC), Barcelona, Catalonia, Spain*
[12]*Lawrence Livermore National Laboratory, Livermore, California 94550, USA*
[13]*Physikalisches Institut, University of Bonn, 53115 Bonn, Germany*
[14]*Istituto Nazionale di Fisica Nucleare (INFN), Sezione di Padova, 35131 Padova, Italy*
[15]*Institute for Optics and Quantum Electronics, Friedrich Schiller University Jena, Jena, Germany*
[16]*Physics Department and Columbia Astrophysics Laboratory, Columbia University, New York, New York 10027, USA*
[17]*Department of Physics and Astronomy, University of British Columbia, Vancouver, British Columbia, Canada*
[18]*Xi'An Jiaotong University, School of Science, Xi'An 710049, China*
[19]*Rudjer Bošković Institute, Zagreb, Croatia*
[20]*Istituto Nazionale di Fisica Nucleare (INFN), Sezione di Trieste, Trieste, Italy*
[21]*Faculty of Physics and Center for Micro and Nano Sciences and Technologies, University of Rijeka, 51000 Rijeka, Croatia*
[22]*Universität Hamburg, Hamburg, Germany*
[23]*Institute of Experimental Physics, University of Hamburg, 22761 Hamburg, Germany*
[24]*Center for Axion and Precision Physics Research, Institute for Basic Science (IBS), Daejeon 34141, Republic of Korea*
[25]*Department of Information and Communications Technologies, Technical University of Cartagena, 30203—Murcia, Spain*
[26]*Istanbul University-Cerrahpasa, Department of Mechanical Engineering, Avcilar, Istanbul, Turkey*
[27]*Boğaziçi University, Physics Department, Bebek, Istanbul, Turkey*
[28]*Extreme Light Infrastructure - Nuclear Physics (ELI-NP), 077125 Magurele, Romania*

[29]*Department of Physics, Korea Advanced Institute of Science and Technology (KAIST),*
Daejeon 34141, Republic of Korea
[30]*Max-Planck-Institut für Sonnensystemforschung, 37077 Göttingen, Germany*

Hypothetical axions provide a compelling explanation for dark matter and could be emitted from the hot solar interior. The CERN Axion Solar Telescope has been searching for solar axions via their back conversion to x-ray photons in a 9-T 10-m long magnet directed toward the Sun. We report on an extended run with the International Axion Observatory pathfinder detector, doubling the previous exposure time. The detector was operated with a xenon-based gas mixture for part of the new run, providing technical insights for future configurations. No counts were detected in the 95% signal-encircling region during the new run, while 0.75 were expected. The new data improve the axion-photon coupling limit to 5.8×10^{-11} GeV^{-1} at 95% CL (for $m_a \lesssim 0.02$ eV), the most restrictive experimental limit to date.

Introduction—Very light pseudoscalar bosons, generically called axionlike particles (ALPs), appear in many motivated extensions of the standard model [1,2]. The paradigmatic example in this category is the axion, whose existence follows from the Peccei-Quinn mechanism as an explanation for why QCD (quantum chromodynamics) is perfectly time-reversal invariant within current experimental precision [3–5]. Axions and ALPs can be dark matter in the form of classical field oscillations that were excited in the early Universe by the realignment mechanism [6–8] or by the decay of topological defects of the axion field [9].

There is a growing international program of experiments in search of these particles [10]. As dark matter components, they could be detected by a number of techniques, each of them optimized for a different axion mass m_a range. Most notably, Sikivie-type axion haloscopes [11] and in particular the Axion Dark Matter Experiment [12], have achieved sensitivity to QCD axion models in the range of $m_a \sim$ few μeV. Independently of the dark matter assumption, axions can be produced and detected in the laboratory, as new forces mediated by them [13] or in light-shining-through-wall experiments like ALPSII at Deutsches Elektronen-Synchrotron DESY [14]. Axions can also be produced in stellar interiors, effectively draining energy and affecting the star's life span. These arguments provide restrictive limits on axion properties, and in some cases may even suggest new energy loss channels [15]. Axions produced in the Sun offer another important

opportunity for detection in the laboratory in experiments dubbed axion helioscopes [11], the topic of this Letter.

A most common strategy to search for axions relies on their generic two-photon coupling. It is given by the vertex

$$\mathcal{L}_{a\gamma} = -\frac{1}{4} g_{a\gamma} F^{\mu\nu} \tilde{F}_{\mu\nu} a = g_{a\gamma} \mathbf{E} \cdot \mathbf{B} a, \tag{1}$$

where a is the axion field, F the electromagnetic field-strength tensor, $g_{a\gamma}$ the coupling constant, $\mathbf{E}$ the electric field, and $\mathbf{B}$ the magnetic field. This vertex enables the decay $a \to \gamma\gamma$, as well as the Primakoff production in stars, i.e., the $\gamma \to a$ scattering in the Coulomb fields of charged particles in the stellar plasma, and the coherent conversion $a \leftrightarrow \gamma$ in laboratory or astrophysical B fields [11,16].

Solar axions can be produced in several processes, depending on their model-dependent interaction channels. We specifically consider axion production by Primakoff scattering of thermal photons deep in the Sun, a process that depends on the coupling constant $g_{a\gamma}$, which is also used for detection. Following this principle, axion helioscopes make use of a dipole magnet directed at the Sun to convert axions to x rays.

This detection concept has been followed by the CERN Axion Solar Telescope (CAST), the most powerful axion helioscope built so far [17]. CAST was in operation at CERN from 2003 until 2021. During this time, the experiment went through different phases and released a number of results, including a first phase using evacuated magnet bores [18,19], followed by "gas phases" with ^{4}He [20,21] and ^{3}He [22,23], to cover sensitivity to higher m_a values. Later on, CAST returned to evacuated magnet bores but with an improved detection line, dubbed the IAXO (International Axion Observatory) pathfinder, that combined a new Micromegas detector with lower background levels, as well as a new x-ray telescope built specifically for axion searches [24] that is based on technology developed for the Nuclear Spectroscopic Telescope Array [25]. This allowed CAST to produce what is at present the strongest

*Contact author: cmargalejo@unizar.es
†Contact author: Jaime.Ruz@cern.ch
‡Deceased.

experimental upper bound to the solar axion-photon coupling [17].

CAST also produced constraints to other (non-Primakoff) axion or ALP production channels in the Sun [26–28], as well as to chameleons [29] and hidden photons [30]. In a later stage, CAST expanded its scope to the search for dark matter axions [31,32] and solar chameleons via pressure sensing [33].

In this last phase, the IAXO pathfinder line kept operating from September 2019 to June 2021 in order to improve the statistics of the 2017 result. As a novelty, part of these data were taken with a new gas recirculation and filtering system to use a Xe-based gas mixture for the Micromegas detectors. The goal was to get lower background for the science analysis by testing this gas filling the Micromegas detector volume in real experiment conditions, which will be valuable for future Xe-based detectors. The analysis of the data taken in these runs is the main result of this Letter. These new results are combined with the latest GridPix data from October 2017 to December 2018. The GridPix detector [34] is optimized for lower energy signals (i.e., it is more sensitive to axion-electron coupling g_{ae}) due to a lower energy threshold than Micromegas detectors as GridPix can detect individual electrons, and its results will be detailed in a forthcoming publication currently in preparation. Here, these data only improved the result marginally in the upper limit for $g_{a\gamma}$.

Experimental setup—The CAST helioscope makes use of a decommissioned prototype LHC magnet [35] of length 9.26 m and a magnetic field of up to 9 T. It has two 4.3 cm diameter cold bores and can have detectors installed on both ends (sunrise and sunset side). It can track the Sun during sunrise and sunset for a total of 3 h per day. A more detailed description can be found in [17,19], and some relevant differences with the current setup, and how they affect the overall efficiency, are described in the Supplemental Material [36].

For the present data taking campaign, a single ultralow background microbulk Micromegas detector [40,41] was installed on the sunrise side of the experiment. This detector is made from electroformed copper and Kapton, has a 3 cm drift distance, an x-ray transparent 4 μm aluminized mylar window acting as cathode and a high granularity 6 × 6 cm stripped readout as anode, with 120 × 120 strips or channels of 0.5 mm pitch. Active and passive shieldings were installed. The active shielding consisted of a plastic scintillator placed above the detector for cosmic muons detection via coincidence. The passive shielding was a lead box surrounding the detector with 10 to 15 cm thick walls to protect the detector from environmental gammas. The detector was coupled to the x-ray telescope, which is optimized for solar axion searches, maximizing its throughput in the ∼3 keV energy range. The whole line, including optics and detector, is described in [24].

In CAST, argon mixtures were used historically as gas in the Micromegas chamber due to being well-studied and posing little engineering challenges [17,27,42], and it was also used during the first period of the data taking discussed in this Letter. However, argon's x-ray fluorescence around 3 keV results in an increased background level at the energy range where the maximum of solar axion Primakoff flux is expected. Consequently, there has been a shift toward exploring alternative gas mixtures, particularly those based on xenon. Unlike the argon mixtures, which were utilized in an open loop system, xenon mixtures were employed in a closed loop system. Special attention has been given to potential contamination of water vapor or oxygen from leaks or outgassing. Implementing this change required the development of a new and more sophisticated gas recirculation system, incorporating moisture and oxygen filters, a recirculation pump and a buffer volume. The gas mixtures used during the last data taking campaign were Ar + 2.3% isobutane at 1.4 bar and 48.85% Xe + 48.85% Ne + 2.3% isobutane at 1.05 bar. Xenon-based gas mixtures have a higher detection efficiency, allowing for the use of lower pressures that reduces the pressure difference between the vacuum pipe and the Micromegas gas volume, which would allow the use of thinner windows with a higher x-ray transparency, increasing the overall efficiency. We demonstrate that their use is possible, paving the way for the future use of even thinner windows and reduced gas pressures.

Data taking—Calibration of the detector was performed at different energies in the CAST x-ray tube at CERN using both Ar- and Xe-based mixtures, providing information on its response to photons of different energies that was later used for event discrimination. During the data taking periods at CAST, calibrations using the 5.9 keV peak of a ^{55}Fe source were taken on a daily basis. This enabled the calibration of each background and tracking run in energy and the evaluation of the detector performance, stability, and energy threshold over time. Once the detector was placed in CAST, the correct alignment of the full beamline was verified by placing a ∼3 keV x-ray generator on the opposite side of the magnet. In addition to these measurements, targets were securely positioned during geometric surveys, allowing for verification of the detector's position. Furthermore, the Sun can be filmed twice per year with an optical telescope and a camera attached to the magnet, ensuring the pointing accuracy of the setup.

The data can be classified in three datasets as listed in Table I, two of them using argon and one using xenon. The argon data are split into two separate datasets because they were taken a few months apart and using different electronics parameters. Each of the three datasets has data obtained under axion-sensitive conditions—namely during tracking, i.e., when the magnet is powered and oriented toward the Sun—as well as data taken under background conditions, i.e., magnet powered on but not pointing to the

TABLE I.   Datasets of the presented data taking campaign. Ar: 97.7% Ar + 2.3% isobutane at 1.4 bar; Xe: 48.85% Xe + 48.85% Ne + 2.3% isobutane at 1.05 bar. The software efficiency ϵ_s at 5.9 keV is indicated for each dataset.

Dataset	Background exposure (h)	Background level (2,7) keV ($\times 10^{-6}$ keV^{-1} cm^{-2} s^{-1})	Tracking exposure (h)	Gas	ϵ_s at 5.9 keV	Years
1	2476	1.7 ± 0.1	130	Ar	80%	2019–2020
2	335	2.3 ± 0.4	25.6	Ar	80%	2020
3	3416	1.5 ± 0.1	159	Xe	90%	2020–2021
Total	6227		314.6			

Sun. The total tracking exposure is 314.6 h and about 20 times more statistics is available for background. Dataset 3 uses optimized parameters of the electronics based on insights gained from the analysis of datasets 1 and 2. This allowed us to reach higher software efficiency ϵ_s by saving the information of all the readout channels each time there was a trigger instead of saving only the information of the channels over the energy threshold.

The detector was stable during most of the data taking campaign and showed an energy resolution of 20% to 23% at 5.9 keV. For datasets 1 and 2 the gain variation was 3.3%, with an energy threshold consistently below 0.4 keV. Dataset 3 required more attention to maintain optimal gas gain and transparency due to the recirculation system and its effect on the gas quality. Consequently, voltage and flow parameters were dynamically adjusted as required. The range of gain variation was 2.5% to 9%. Since the gain changes are constantly monitored they can be easily corrected with every calibration and they do not affect the data quality and analysis. The energy threshold remained below 0.75 keV for most (83%) of the runs. A more detailed overview of the data taking stability is provided in the Supplemental Material [36].

Data analysis and results—The data analysis and background rejection was performed using the REST-for-physics framework [43,44], a ROOT-based collaborative software developed for data analysis and Geant4-based [45] simulations of rare event searches experiments and gaseous detectors using time projection chambers. This analysis was performed in a fully blind manner to prevent bias in the results.

The data analysis chain turns the raw data into events with a given energy and a physical position on the readout plane, for which topological observables can be computed. This allows for powerful background rejection as x rays (small, symmetric, pointlike, and single-track events) are easily identified. Furthermore, events that occur in coincidence with a cosmic event in the active shielding are also removed. See [46] and also the Supplemental Material [36] for an overview of the Micromegas events analysis and definition of the x-ray selection algorithms.

In this Letter, a background rejection taking into account calibrations taken at six different energies (1.5, 2.1, 3.0, 4.5, 5.9, and 8.0 keV) in an x-ray tube with interchangeable targets to produce the different energies, has been implemented. This approach is used instead of relying solely on the peak obtained in the daily calibrations with the ^{55}Fe source at CAST. This allowed us to consider the energy dependence of the observables' distributions, and adapt the x-ray cuts for each energy range accordingly. This approach ensured that the figure of merit $\epsilon_{sg}/\sqrt{b}$, where ϵ_{sg} is the efficiency of the cuts when applied to the signal data and b is the background rate after cuts, is maximized in every range independently. As a result, we achieved the highest software efficiencies to date using Micromegas detectors, ranging from 70% to 90% depending on the energy of the event. This improvement is especially noticeable at energies away from the 5.9 keV peak of ^{55}Fe, as we could now use information at other energies based on the runs in x-ray tube that help us better define x-ray-like events of any energy. There have also been improvements in the hardware efficiency. A 4 μm polypropylene differential window previously installed in [17], which had a low x-ray transparency at low energies, was removed for this run, thus significantly increasing the efficiency at low energies. The use of Xe-based gas mixtures also provides a higher detection efficiency in the energy range of interest in addition to avoiding the argon fluorescence peak at ~3 keV. Furthermore, the detector response has been taken into account, which also increases slightly the efficiency. Overall, the efficiency has been improved by a factor of 2 with respect to previous works, in particular [17], concentrated at low energies. A more detailed description of the improved efficiencies is provided in the Supplemental Material [36].

The background level achieved during the discussed campaign is based on 6227 h of total data, divided in three different datasets listed in Table I. Most of the data belong to datasets 1 (Ar-based) and 3 (Xe-based), with a background level of $(1.7 \pm 0.1) \times 10^{-6}$ keV^{-1} cm^{-2} s^{-1} and $(1.5 \pm 0.1) \times 10^{-6}$ keV^{-1} cm^{-2} s^{-1}, respectively. The background with xenon is the lowest in the energy region of interest due to the absence of the 3 keV fluorescence peak (Fig. 1), which is an important achievement for solar axion searches as it directly impacts the experiment's sensitivity, pushing it to the best levels to date. Dataset 2 is a smaller argon dataset in which we started saving the information of all the readout channels even if they were below the energy threshold. It has a slightly higher background rate of
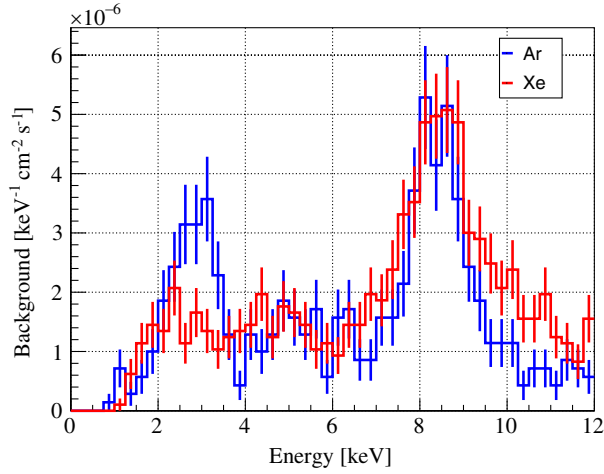
FIG. 1. Energy distribution of background counts in the inner 20 mm diameter circular region of the detector in dataset 1 (blue line, labeled Ar) and dataset 3 (red line, labeled Xe). The y axis is in normalized counts $keV^{-1}\,cm^{-2}\,s^{-1}$. The 8 keV peak due to copper is seen in both spectra, but the $\sim$3 keV Ar fluorescence peak is not present when using xenon. This increases the signal-to-noise ratio in an energy region where the expected signal is maximal.
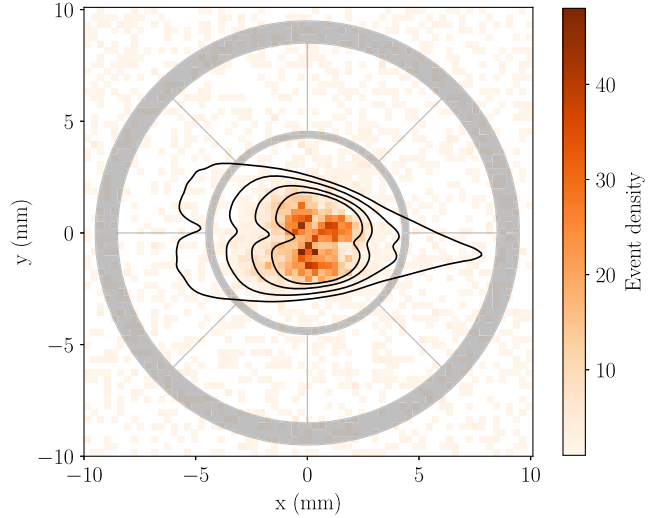

FIG. 2. 2D hit map of detected counts in the Micromegas detector plane during the calibration run with the source placed at the far end of the magnet, so the emitting x rays cross the full beamline, and are focused by the optics. The distribution is overlaid with the 68%, 85%, 95%, and 99% contours of the simulated ray tracing (black lines). These data are used to determine the translation and rotation of the expected focused signal on the 2D detector plane. The shade of the copper strongback of the x-ray window will block some of the signal and it is plotted as a gray shade.

$(2.3 \pm 0.4) \times 10^{-6}$ $keV^{-1}\,cm^{-2}\,s^{-1}$, but it is statistically compatible with the background level of dataset 1.

This background level is compared to the rate of x-ray-like observed events during the 314.6 h of solar tracking time. The same selection algorithms are applied to these data and the aim is to look for any x-ray event excess during axion-sensitive conditions. In order to do so, ray tracing simulations provide the information of the signal spot shape and position on the readout plane. The signal probability density function (PDF) is energy dependent, but most of the flux is in all cases focused into an area of a few mm^2. The ray-tracing simulations were performed for a solar axion flux originating from an extended source with and angular size equivalent to the solar core, placed at infinity. Simulations were also conducted for an x-ray source like the one used for alignment calibrations, originating from a point source placed at 10 m distance. Comparing the latter with the real data allows to align the simulations density contours with the experimental data (Fig. 2). For this purpose, the contours containing 68%, 85%, 95%, and 99% of the signal were computed. The same alignment was applied to the x-ray events during tracking (Fig. 3), where we observe 0 counts in the energy range of interest (2 to 7 keV) in the 95% signal-encircling region in all three datasets, while expectations based on the background rate and exposure time is 0.75 counts.

Limit on the axion-photon coupling—We use an unbinned likelihood method to compute an upper limit on $g_{a\gamma}$, following the same methodology as in [17,21–23], as it is better suited for low count experiments. The defined likelihood function is
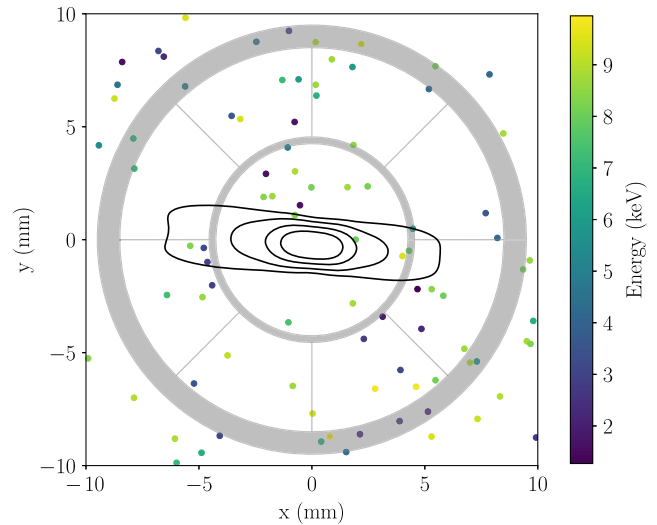

FIG. 3. 2D hit map of the detected events during all the tracking runs in axion-sensitive conditions, during all three datasets considered in this Letter. The color of each dot represents its energy according to the scale on the right. The overlaid black lines represent the 68%, 85%, 95%, and 99% signal-encircling regions, according to the ray-tracing simulation of the optics. The window strongback is overlaid as a gray shade as in Fig. 2.

$$\ln \mathcal{L} = -R_T + \sum_{1}^{n} \ln R(E_i, \overrightarrow{x_i}), \qquad (2)$$

where $R_T = s(g_{a\gamma}) + b$ is the sum of the expected number of signal counts $s(g_{a\gamma})$ based on the experimental setup, solar model and coupling constant, and background counts b based on the background rate. The sum term goes over n tracking events and it encodes the signal and background expected rates at energy E_i and position $\overrightarrow{x_i}$ of event i, such that

$$R(E_i, \overrightarrow{x_i}) = s(E_i, \overrightarrow{x_i}) + b(E_i). \qquad (3)$$

Here, the background rate $b(E_i)$ is energy dependent (Fig. 1) but it is considered spatially uniform, whereas the signal rate $s(E_i, \overrightarrow{x_i})$ depends on the position as well as the energy, as illustrated by the contours of the ray-tracing simulation in Fig. 3. This signal rate is given by

$$s(E_i, \overrightarrow{x_i}) = \frac{d\Phi_a}{dE} P_{a\to\gamma} \epsilon(E, \overrightarrow{x_i}), \qquad (4)$$

where the detector response as a function of energy is encoded in the $\epsilon(E, \overrightarrow{x_i})$ term, which includes the x-ray optics efficiency of the telescope, the hardware and software efficiencies, and the axion signal simulations defining the expected signal distribution (Fig. 3). The axion to photon conversion probability in an homogeneous magnetic field B of length L in vacuum is

$$P_{a\to\gamma} = \left(g_{a\gamma} B \frac{\sin(qL/2)}{q} \right)^2, \qquad (5)$$

where $q = m_a^2/2E$ is the momentum transfer between axion and photon in vacuum. Finally, the differential Primakoff solar axion flux in $\mathrm{keV^{-1} \, cm^{-2} \, s^{-1}}$ is given by the expression [19]

$$\frac{d\Phi_a}{dE} = 6.02 \times 10^{10} g_{10}^2 E^{2.481} e^{-\frac{E}{1.205}}, \qquad (6)$$

where $g_{10} = g_{a\gamma}/(10^{-10} \, \mathrm{GeV^{-1}})$ and energy E is in keV.

The Bayesian posterior probability $\mathcal{P}(g_{a\gamma})$ is obtained from the likelihood function in Eq. (2) by $\mathcal{P} = \mathcal{L} \times \Pi$, where $\Pi(g_{a\gamma})$ is the prior probability that is chosen to be flat in $g_{a\gamma}^4$ for positive values and $\Pi = 0$ for negative ones.

The resulting PDF is combined with results from [17], which uses data up to 2015 and serves as the benchmark for the axion-photon coupling set by CAST. Additionally, data from the 2017–2018 campaign with a GridPix detector [34,42], providing an extra 160 h of data, is included. This combination allowed us to create an overall PDF that encapsulates all CAST data with sensitivity to $g_{a\gamma}$.

Because of the absence of a significant excess of events over background, these data are consistent with no axion
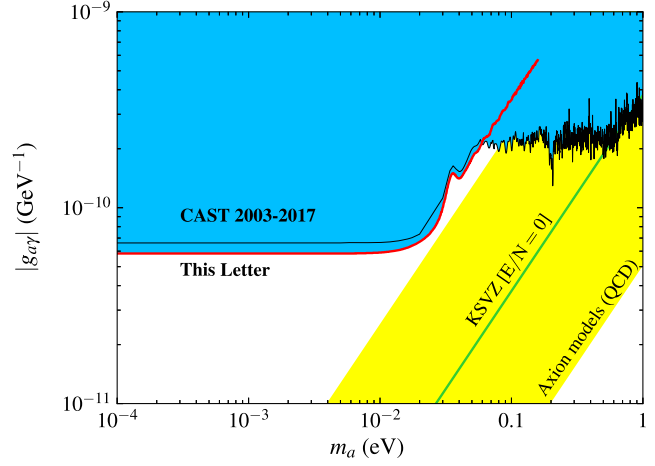

FIG. 4. Parameter space for axions and ALPs showing the latest constraints in $g_{a\gamma}$. The red line indicates the region excluded by this work, which builds upon the former limit indicated in black. The yellow band represents the region QCD axion models point to.

signal. Thus, an upper limit to $g_{a\gamma}$ is set by integrating the posterior probability $\mathcal{P}$ from 0% to 95%. The analysis is repeated for different m_a values to compute the exclusion line shown in red in Fig. 4, which is the resulting line of combining the current result with the aforementioned past data taking campaigns.

For $m_a \lesssim 0.02$ eV, the upper limit is set to

$$g_{a\gamma} < 5.8 \times 10^{-11} \, \mathrm{GeV^{-1}} \quad \text{at } 95\% \, \mathrm{CL}. \qquad (7)$$

For higher axion masses up to 0.06 keV we have also set the most stringent limit, getting closer to the QCD axion band. For $m_a \gtrsim 0.06$ eV, the data taken during the ^{4}He and ^{3}He as buffer gas periods is still the most competitive result from CAST [18–20]. The uncertainty in this latest result is dominated by the statistical effect of the low count rate available. The effect of systematic errors on this limit is discussed in the Supplemental Material [36] but remains well below 10% of the statistical uncertainty of the result.

This result is a mild statistical underfluctuation as compared to the expected sensitivity of the experiment, defined as the median upper limit of multiple Monte Carlo simulations, which for the current exposure time is $g_{a\gamma} < 0.59 \times 10^{-10} \, \mathrm{GeV^{-1}}$. See the Supplemental Material [36] for a more detailed explanation of the simulations of the experiment's potential sensitivity.

Conclusions—The result presented in this Letter represents the new best limit on $g_{a\gamma}$ in the range $m_a \lesssim 0.02$ eV, superseding our previous best result, and going beyond the limit derived from the energy loss of horizontal branch stars [47,48]. Currently, our bound is surpassed only by astrophysical considerations on the axion impact on the R2 parameter in globular clusters, which lead to $g_{a\gamma} < 0.47 \times 10^{-10} \, \mathrm{GeV^{-1}}$. This last result, however, relies on the accurate counting of stars in globular clusters as well as on numerical simulations of

stars in late evolutionary stages, and is marred by considerably larger uncertainties. This improvement originates not only from the additional statistics, but also from an improved detection efficiency, especially at low energies. This is in part thanks to the use of a Xe-based gas mixture in the Micromegas detector gas volume, something that also improves the background in the region of interest. This aspect constitutes a relevant technical achievement that provides useful operational experience for future similar implementations in BabyIAXO and IAXO.

The improved energy threshold achieved and the more controlled low energy response of the detector are also of interest to search for other solar axion production channels at the lower energy range, like the g_{ae}-mediated "ABC" solar axions, something that will be the scope of forthcoming work.

Given that CAST definitively stopped operation in 2021, the new bound on $g_{a\gamma}$ here presented will remain as the legacy result on solar axions, until new results come online once the BabyIAXO helioscope, now starting construction at Deutsches Elektronen-Synchrotron DESY, starts producing data.

[1] A. Ringwald, Exploring the role of axions and other WISPs in the dark universe, Phys. Dark Universe **1**, 116 (2012).

[2] J. Jaeckel and A. Ringwald, The low-energy frontier of particle physics, Annu. Rev. Nucl. Part. Sci. **60**, 405 (2010).

[3] R. D. Peccei and H. R. Quinn, *CP* conservation in the presence of instantons, Phys. Rev. Lett. **38**, 1440 (1977).

[4] F. Wilczek, Problem of strong P and T invariance in the presence of instantons, Phys. Rev. Lett. **40**, 279 (1978).

[5] S. Weinberg, A new light boson?, Phys. Rev. Lett. **40**, 223 (1978).

[6] J. Preskill, M. B. Wise, and F. Wilczek, Cosmology of the invisible axion, Phys. Lett. **120B**, 127 (1983).

[7] L. F. Abbott and P. Sikivie, A cosmological bound on the invisible axion, Phys. Lett. **120B**, 133 (1983).

[8] M. Dine and W. Fischler, The not so harmless axion, Phys. Lett. **120B**, 137 (1983).

[9] D. J. E. Marsh, Axion cosmology, Phys. Rep. **643**, 1 (2016).

[10] I. G. Irastorza and J. Redondo, New experimental approaches in the search for axion-like particles, Prog. Part. Nucl. Phys. **102**, 89 (2018).

[11] P. Sikivie, Experimental tests of the invisible axion, Phys. Rev. Lett. **51**, 1415 (1983).

[12] C. Bartram *et al.* (ADMX Collaboration), Search for invisible axion dark matter in the 3.3–4.2 μeV mass range, Phys. Rev. Lett. **127**, 261803 (2021).

[13] A. Arvanitaki and A. A. Geraci, Resonantly detecting axion-mediated forces with nuclear magnetic resonance, Phys. Rev. Lett. **113**, 161801 (2014).

[14] I. Oceano (ALPS II Collaboration), Axion and ALP search with the any light particle search II experiment at DESY, Proc. Sci. EPS-HEP2023 (**2024**) 117.

[15] L. Di Luzio, M. Giannotti, E. Nardi, and L. Visinelli, The landscape of QCD axion models, Phys. Rep. **870**, 1 (2020).

[16] G. Raffelt and L. Stodolsky, Mixing of the photon with low mass particles, Phys. Rev. D **37**, 1237 (1988).

[17] V. Anastassopoulos *et al.* (CAST Collaboration), New CAST limit on the axion-photon interaction, Nat. Phys. **13**, 584 (2017).

[18] K. Zioutas *et al.* (CAST Collaboration), First results from the CERN Axion Solar Telescope (CAST), Phys. Rev. Lett. **94**, 121301 (2005).

[19] S. Andriamonje *et al.* (CAST Collaboration), An improved limit on the axion-photon coupling from the CAST experiment, J. Cosmol. Astropart. Phys. 04 (2007) 010.

[20] E. Arik *et al.* (CAST Collaboration), Probing eV-scale axions with CAST, J. Cosmol. Astropart. Phys. 02 (2009) 008.

[21] M. Arik *et al.* (CAST Collaboration), New solar axion search using the CERN Axion Solar Telescope with ^{4}He filling, Phys. Rev. D **92**, 021101 (2015).

[22] E. Arik *et al.* (CAST Collaboration), Search for Sub-eV mass solar axions by the CERN axion solar telescope with ^{3}He buffer gas, Phys. Rev. Lett. **107**, 261302 (2011).

[23] M. Arik *et al.* (CAST Collaboration), Search for solar axions by the CERN Axion Solar Telescope with ^{3}He buffer gas: Closing the hot dark matter gap, Phys. Rev. Lett. **112**, 091302 (2014).

[24] F. Aznar *et al.*, A Micromegas-based low-background X-ray detector coupled to a slumped-glass telescope for axion research, J. Cosmol. Astropart. Phys. 12 (2015) 008.

[25] F. A. Harrison *et al.*, The Nuclear Spectroscopic Telescope Array (NuSTAR) high-energy X-ray mission, Astrophys. J. **770,** 103 (2013).

[26] S. Andriamonje *et al.* (CAST Collaboration), Search for 14.4 keV solar axions emitted in the M1-transition of ^{57}Fe nuclei with CAST, J. Cosmol. Astropart. Phys. 12 (2009) 002.

[27] K. Barth *et al.* (CAST Collaboration), CAST constraints on the axion-electron coupling, J. Cosmol. Astropart. Phys. 05 (2013) 010.

[28] S. Andriamonje *et al.* (CAST Collaboration), Search for solar axion emission from ^{7}Li and $D(p,\gamma)^{3}$He nuclear decays with the CAST γ-ray calorimeter, J. Cosmol. Astropart. Phys. 03 (2010) 032.

[29] V. Anastassopoulos *et al.* (CAST Collaboration), Search for chameleons with CAST, Phys. Lett. B **749,** 172 (2015).

[30] J. Redondo, Atlas of solar hidden photon emission, J. Cosmol. Astropart. Phys. 07 (2015) 024.

[31] A. Alvarez-Melcón *et al.* (CAST Collaboration), First results of the CAST-RADES haloscope search for axions at 34.67 µeV, J. High Energy Phys. 10 (2020) 075.

[32] C. M. Adair *et al.* (CAST Collaboration), Search for dark matter axions with CAST-CAPP, Nat. Commun. **13,** 6180 (2022).

[33] S. Arguedas-Cuendis *et al.* (CAST Collaboration), First results on the search for chameleons with the KWISP detector at CAST, Phys. Dark Universe **26,** 100367 (2019).

[34] C. Krieger, J. Kaminski, and K. Desch, InGrid-based X-ray detector for low background searches, Nucl. Instrum. Methods Phys. Res., Sect. A **729,** 905 (2013).

[35] K. Zioutas *et al.*, A decommissioned LHC model magnet as an axion telescope, Nucl. Instrum. Methods Phys. Res., Sect. A **425,** 480 (1999).

[36] See Supplemental Material at http://link.aps.org/supplemental/10.1103/PhysRevLett.133.221005 for data taking and analysis summary, explanation of the efficiencies and systematic effects, and expected sensitivity, which includes Refs. [37–39].

[37] J. K. Vogel, Searching for solar axions in the eV-mass region with the CCD detector at CAST, Ph.D. thesis, Albert-Ludwigs-Universität Freiburg, Freiburg, 2009.

[38] S. Hoof, J. Jaeckel, and L. J. Thormaehlen, Quantifying uncertainties in the solar axion flux and their impact on determining axion model parameters, J. Cosmol. Astropart. Phys. 09 (2021) 006.

[39] G. Cowan, K. Cranmer, E. Gross, and O. Vitells, Asymptotic formulae for likelihood-based tests of new physics, Eur. Phys. J. C **71,** 1554 (2011).

[40] Y. Giomataris, P. Rebourgeard, J. P. Robert, and G. Charpak, MICROMEGAS: A high-granularity position-sensitive gaseous detector for high particle-flux environments, Nucl. Instrum. Methods Phys. Res., Sect. A **376,** 29 (1996).

[41] S. Andriamonje *et al.*, Development and performance of microbulk Micromegas detectors, J. Instrum. **5,** P02001 (2010).

[42] S. Schmidt, Search for solar axions using a 7-GridPix IAXO prototype detector at CAST, Ph.D. thesis, Universität Bonn, Bonn, 2024.

[43] K. Altenmüller *et al.*, REST-for-physics, a ROOT-based framework for event oriented data analysis and combined Monte Carlo response, Comput. Phys. Commun. **273,** 108281 (2022).

[44] REST-for-Physics, a ROOT-based framework for event oriented data analysis and combined Monte Carlo response [GitHub repository], https://github.com/rest-for-physics.

[45] S. Agostinelli *et al.*, Geant4—a simulation toolkit, Nucl. Instrum. Methods Phys. Res., Sect. A **506,** 250 (2003).

[46] K. Altenmüller *et al.*, Revisiting the bound on axion-photon coupling from globular clusters, Front. Phys. **12,** 1384415 (2024).

[47] A. Ayala, I. Dominguez, M. Giannotti, A. Mirizzi, and O. Straniero, An improved bound on axion-photon coupling from Globular Clusters, Phys. Rev. Lett. **113,** 191302 (2014).

[48] O. Straniero, A. Ayala, M. Giannotti, A. Mirizzi, and I. Dominguez, Axion-photon coupling: Astrophysical constraints, Report No. DESY-PROC-2015-02, 77-81, 2015, http://inspirehep.net/record/1511517/files/fulltext.pdf.